

The Vimos VLT Deep Survey:

Global properties of 20000 galaxies in the $I_{AB} < 22.5$ WIDE survey

B. Garilli¹, O. Le Fèvre², L. Guzzo⁹, D. Maccagni¹, V. Le Brun², S. de la Torre², B. Meneux^{1,9}, L. Tresse², P. Franzetti¹, G. Zamorani³, A. Zanichelli⁴, L. Gregorini⁴, D. Vergani¹, D. Bottini¹, R. Scaramella^{4,13}, M. Scodreggio¹, G. Vettolani⁴, C. Adami², S. Arnouts^{22,2}, S. Bardelli³, M. Bolzonella³, A. Cappi³, S. Charlot^{8,10}, P. Ciliegi³, T. Contini⁷, S. Foucaud²¹, I. Gavignaud¹², O. Ilbert²⁰, A. Iovino⁹, F. Lamareille⁷, H.J. McCracken^{10,11}, B. Marano⁶, C. Marinoni¹⁸, A. Mazure², R. Merighi³, S. Paltani^{15,16}, R. Pelló⁷, A. Pollo^{2,17}, L. Pozzetti³, M. Radovich⁵, E. Zucca³, Blaizot, J.²³, A. Bongiorno²¹, O. Cucciati^{9,14}, Y. Mellier^{10,11}, C. Moreau², and L. Paioro¹

(Affiliations can be found after the references)

Received ...; accepted ...

ABSTRACT

Context. The VVDS-Wide survey has been designed with the general aim of tracing the large-scale distribution of galaxies at $z \sim 1$ on comoving scales reaching $\sim 100h^{-1} \text{ Mpc}$, while providing a good control of cosmic variance over areas as large as a few square degrees. This is achieved by measuring redshifts with VIMOS at the ESO VLT to a limiting magnitude $I_{AB} = 22.5$, targeting four independent fields with size up to 4 deg^2 each.

Aims. We discuss here the survey strategy which covers 8.6 deg^2 and present the general properties of the current redshift sample. This includes 32734 spectra in the four regions, covering a total area of 6.1 deg^2 with a sampling rate of 22 to 24%. This paper accompanies the public release of the first 18143 redshifts of the VVDS-Wide survey from the 4 deg^2 contiguous area of the F22 field at $RA=22^h$.

Methods. We have devised and tested an objective method to assess the quality of each spectrum, providing a compact figure-of-merit, particularly effective in the case of long-lasting spectroscopic surveys with varying observing conditions. Our figure of merit is a measure of the robustness of the redshift measurement and, most importantly, can be used to select galaxies with uniform high-quality spectra to carry out reliable measurements of spectral features. We use the data available over the four independent regions to directly measure the variance in galaxy counts. We compare it with general predictions from the observed galaxy two-point correlation function at different redshifts and with that measured in mock galaxy surveys built from the Millennium simulation.

Results. The purely magnitude-limited VVDS Wide sample includes 19977 galaxies, 304 type I AGNs, and 9913 stars. The redshift success rate is above 90% independently of magnitude. A cone diagram of the galaxy spatial distribution provides us with the current largest overview of large-scale structure up to $z \sim 1$, showing a rich texture of over- and under-dense regions. We give the mean $N(z)$ distribution averaged over 6.1 deg^2 for a sample limited in magnitude to $I_{AB} = 22.5$. Comparing galaxy densities from the four fields shows that in a redshift bin $\Delta z = 0.1$ at $z \sim 1$ one still has factor-of-two variations over areas as large as $\sim 0.25 \text{ deg}^2$. This level of cosmic variance agrees with that obtained by integrating the galaxy two-point correlation function estimated from the F22 field alone. It is also in fairly good statistical agreement with that predicted by the Millennium mocks.

Conclusions. The VVDS WIDE survey provides the currently largest area coverage among redshift surveys reaching $z \sim 1$. The variance estimated over the survey fields shows explicitly how clustering results from deep surveys of even 1 deg^2 size should be interpreted with caution. The survey data represent a rich data base to select complete sub-samples of high-quality spectra and to study galaxy ensemble properties and galaxy clustering over unprecedented scales at these redshifts. The redshift catalog of the 4 deg^2 F22 field is publicly available at <http://cencosw.oamp.fr>.

Key words. Galaxies: fundamental parameters - Cosmology: observations - Cosmology: large-scale structure of the Universe - Astronomical data bases: Catalogs

1. Introduction

The large-scale distribution of galaxies contains unique information on the structure of our Universe and the fundamental parameters of the cosmological model. The relation of galaxy properties to large-scale structure in turn provides important clues on the physics of galaxy formation within the standard paradigm in which baryons are assembled inside dark-matter halos (e.g. White & Rees 1978). Redshift surveys of the “local” ($z < 0.2$) Universe as the 2dFGRS (Colless et al. 2001) and SDSS (Abazajian et al. 2003) contain several hundred thousand galaxies spanning a few thousands square degrees. These large

samples and explored volumes have allowed large-scale structure studies to be pushed well into the linear regime $r \gg 5 h^{-1} \text{ Mpc}$ while having at the same time a detailed characterization of small-scale clustering and its dependence on galaxy properties like luminosity, colour and morphology (e.g. Madgwick et al. 2003; Norberg et al. 2001, 2002; Zehavi et al. 2005; Li et al. 2006). All these features and properties are expected to depend on redshift, and different evolutionary paths can lead to similar observational properties in the local universe. Ideally, one would like to be able to gather similarly large samples over comparably large volumes, at cosmologically relevant distances ($z \gg 0.3$). First pioneering deep redshift surveys capable of measuring the evolution of clustering go back to the 1990’s and were

limited to a few hundred square arcminutes (e.g. Le Fèvre et al. 1996; Shepherd et al. 2001). Even deeper measurements of clustering evolution were provided by specific color-selected surveys, using the Lyman-break technique, although these give a very biased view of large-scale structure limited to a specific class of objects (e.g. Steidel et al. 1998). More recent surveys like GOODS (e.g. Giavalisco et al. 2004) and DEEP (e.g. Koo 1995) provide extended multi-wavelength coverage, but are still limited to small fields. Only recently, thanks to the increased multi-plexing ability of spectrographs mounted on 10-m class telescopes, robust clustering studies of the general galaxy population at $z \sim 1$ have become feasible. This opportunity has been exploited by the VVDS (Le Fèvre et al. 2005c) and the DEEP2 (Davis et al. 2003) surveys. The VVDS Deep sample (Le Fèvre et al. 2005c), in particular, covered a reasonably large area ($\sim 0.5 \text{ deg}^2$) up to redshift 4 and to a very deep magnitude limit ($I_{AB} = 24$). Major clustering results using these data have included studies of the evolution of galaxy clustering since $z \sim 2$ (Le Fèvre et al. 2005a), its dependence on luminosity, spectral type and stellar mass (Pollo et al. 2006; Meneux et al. 2006, 2008) and the evolution and non-linearity of galaxy bias (Marinoni et al. 2005), together with a direct assessment of the evolution of environmental effects, as the dependence of colour (Cucciati et al. 2006) or luminosity function (Ilbert et al. 2005; Zucca et al. 2006; Ilbert et al. 2006) on local density. Still, the area surveyed by the VVDS Deep is not yet large enough to fully characterize large-scale structure at high redshift: results from 2dF show that structures of size $\sim 50 h^{-1} \text{ Mpc}$ do exist in the local Universe, while in the VVDS-Deep itself a structure at $z \sim 0.9$ is found to fill the full survey field ($\sim 14 h^{-1} \text{ Mpc}$) (Le Fèvre et al. 2005b). The *Wide* part of the VVDS survey has been conceived specifically to improve upon this, covering structures with size $\sim 50 h^{-1} \text{ Mpc}$ at $z \sim 1$, while having the ability to measure the variance in galaxy density on scales of a few square degrees. This will be achieved by measuring redshifts to $I_{AB} = 22.5$ over four separated fields on the sky, with size up to 4 deg^2 each.

In this paper we present a first analysis of the currently available redshifts from the VVDS-Wide spectroscopic survey, including in particular the data collected over the full $\sim 4 \text{ deg}^2$ area of the F22 field, which are publicly released to the scientific community. The paper is organized as follows. In section 2 we describe the VVDS Wide survey strategy and report on the status of the observations conducted so far; in section 3 we assess redshift reliability depending on data quality, in section 4 we present the main characteristics of the resulting redshift catalog, while in section 5 we present the widest cone diagram currently available up to $z \sim 1.0$, quantify the field to field variance of the redshift distribution and how it can affect smaller size surveys and compare the observed cosmic variance with model predictions.

Throughout this paper, we have used a Concordance Cosmology with $\Omega_m = 0.3$, and $\Omega_\Lambda = 0.7$. The Hubble constant is normally parameterized via $h = H_0/100$, while a value $H_0 = 70 \text{ km s}^{-1} \text{ Mpc}^{-1}$ has been used when computing absolute magnitudes.

2. The VVDS Wide survey

The VVDS Wide survey uses VIMOS at the ESO VLT to target 4 separate fields, one of which includes the VVDS Deep survey area, evenly distributed on the sky and covering a total of 16

deg^2 . With a $2 \times 2 \text{ deg}^2$ size, each field can span along the diagonal a transverse comoving size of $116 h^{-1} \text{ Mpc}$ at $z = 1$. The names and coordinates of each field are given in Table 1.

In each of the areas we have excellent photometric coverage, extending from U to K. In addition to the U, *BVRI*, *JK* surveys conducted by the VVDS team (Radovich et al. (2004); McCracken et al. (2003); Iovino et al. (2005)), the sky regions at 02 and 22 hours are also covered by the CFHTLS survey¹ and the UKIDSS survey (Warren et al. 2007). The VVDS Deep field has also been observed at 1.4 GHz at the VLA (Bondi et al. (2003); Ciliegi et al. (2005)), by XMM (Pierre et al. (2004); Chiappetti et al. (2005)), by Galex (Arnouts et al. (2005); Schiminovich et al. (2005)) and by Spitzer (Lonsdale et al. 2003). The spectroscopic sample has been derived from an I selected photometric catalog applying a pure flux limit at $I_{AB} = 22.5$, which provides the best compromise between efficiency in covering a large area and depth of the final spectroscopic sample. A specific choice of the survey was that of not removing stars *a priori* using colour or compactness criteria, to avoid biases against compact galaxies and AGN.

The original plan of the VVDS Wide survey, involved a “two-pass” observing strategy: each of the four areas is covered by two slightly displaced (2 arcmin) grids of adjacent VIMOS pointings (see below for a description of the current implementation of this plan). This strategy allows one to reach a spectroscopic sampling rate of $\sim 35\%$ of all galaxies with $I_{AB} < 22.5$, which is important for density reconstruction studies (Marinoni et al. 2005), while keeping the required observing time within reasonable limits. At the same time, the 2-arcmin shifts is chosen as to fill (at least partially) the gaps left by the VIMOS footprint. For the VVDS Wide survey, the exposure time of each pointing was 45 minutes in MOS mode, using the Low Resolution Red grism. As in the case of the VVDS Deep survey (see Le Fèvre et al. 2005c), we have used a jitter observing sequence, with 5 steps along the slit, each separated by 0.7 arcsec. This strategy allows us to considerably reduce the fringing produced by the CCDs above $\sim 8000 \text{ \AA}$ (LeFevre et al. 2003), although fringing residuals still appear for the brighter and more extended sources, as well as in those observations where seeing was higher than 1.0 arcsec. Observation preparation, mask layout, and observing strategy is the same as for the VVDS Deep sample: using the VMPS software (Bottini et al. 2005), we have been able to place ~ 400 slits on average per VIMOS mask-set down to the limiting magnitude of the VVDS Wide survey. Data have been reduced using the VIMOS Interactive Pipeline and Graphical Interface package (VIPGI Scodreggio et al. 2005).

The observations presented here were collected mostly during Guaranteed Time observations (5 extended visitor observing runs from Oct. 2002 to Sep. 2004), with a small fraction acquired during two further runs in Guest Observer standard time (service runs in February 2006 and 2007). As visually summarized in Fig. 1, we completed the first pass on the 4.0 deg^2 F22 area, plus a second pass on the central $\sim 0.5 \times 0.5 \text{ deg}^2$ of the same field. We further include here the redshift

¹ Based on observations obtained with MegaPrime/MegaCam, a joint project of CFHT and CEA/DAPNIA, at the Canada-France-Hawaii Telescope (CFHT) which is operated by the National Research Council (NRC) of Canada, the Institut National des Science de l’Univers of the Centre National de la Recherche Scientifique (CNRS) of France, and the University of Hawaii. This work is based in part on data products produced at TERAPIX and the Canadian Astronomy Data Centre as part of the Canada-France-Hawaii Telescope Legacy Survey, a collaborative project of NRC and CNRS.

Table 1. VVDS Wide survey field position and observing information

Field	R.A	Dec	Surveyed area	Effective area	N.of pointings	sampling rate
0226-04 (F02)	02h26m00.0s	-04deg30'00"	0.5	0.5	20	24%
1003+01 (F10)	10h03m00.0s	+01deg30'00"	1.9	0.6	11 ¹	24%
1400+05 (F14)	14h00m00.0s	+05deg00'00"	2.2	0.9	17 ²	22%
2217+00 (F22)	22h17m50.4s	+00deg24'00"	4.0	3.0	51	22%

¹For 1 pointing, only 1 quadrant has been reduced so far

²Reduction of 4 pointings is still partial

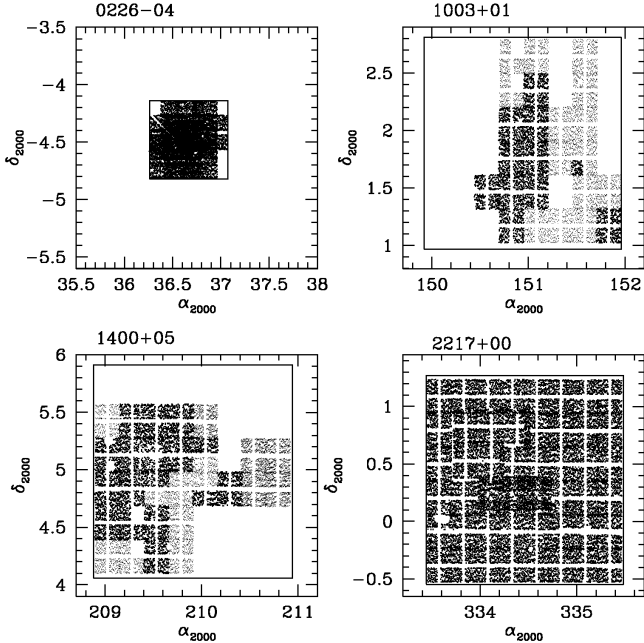


Fig. 1. Layout of observed fields for the VVDS Wide survey: the square represents the planned area to be covered. Black dots correspond to measured redshifts which are used in this paper, while grey dots are from objects which have been observed, but whose redshift is still being finalised. The empty grid corresponds to the VIMOS foot-print, which leaves a 2-arcmin-thick empty cross among the four quadrants. All data for the F02 and F22 fields are public at <http://cencosw.oamp.fr/>.

measurements from the first pass over 0.8 and 1.2 deg^2 in F10 and F14 respectively, while further 2.1 deg^2 in these area are under analysis and are not included in this paper (grey dots in Fig. 1). Finally, we also include redshifts for all galaxies with $I_{AB} < 22.5$ in the 0.5 deg^2 of the F02 field covered by the VVDS-Deep survey to $I_{AB} = 24$. Overall, this data set corresponds to $\sim 36\%$ of the original VVDS Wide survey goal. Given the instrument geometry, with one pass only there are *empty crosses* not covered by the instrument (see Fig. 1, F10, F14 and outer part of F22 areas). In Table 1 we give both the total area covered so far by the VVDS Wide survey, (i.e. the global area covered by either grey or black points in fig. 1), and the *effective* area, i.e. the area including only fully reduced pointings (black points only) and net of the *empty crosses*. In Table 1 we also give the total number of pointings reduced so far for each field, and the average sampling rate of measured redshifts at the given magnitude limit.

3. Redshift measurement, data quality, and reliability

Redshifts have been measured using the same “double-check” procedure described in Le Fèvre et al. (2005c), adopting the same grading scheme to characterize the reliability of the measured redshift:

- flag 4: a 100% secure redshift, with high SNR spectrum and obvious spectral features supporting the redshift measurement;
- flag 3: a very secure redshift, strong spectral features;
- flag 2: a secure redshift measurement, several features in support of the measurement;
- flag 1: a tentative redshift measurement, based on weak spectral features and continuum shape;
- flag 0: no redshift measurement possible, no apparent features;
- flag 9: only one secure single spectral feature in emission, typically interpreted as $[\text{OII}]3727 \text{ \AA}$, or $\text{H}\alpha$.

A similar classification is used for broad line AGN, which we identify as spectra showing at least one “broad line” (i.e. resolved at the spectral resolution of the VVDS). Flags for broad line AGN have the following meaning

- flag 14: secure AGN with 100% secure redshift, at least 2 broad lines;
- flag 13: secure AGN with good confidence redshift, based on one broad line and some faint additional feature;
- flag 19: secure AGN with one single secure emission line feature, redshift based on one line only;
- flag 12: a 100% secure redshift measurement, but lines are not significantly broad, might not be an AGN;
- flag 11: a tentative redshift measurement, spectral features not significantly broad.

Serendipitous objects appearing by chance within the slit of the main target are identified by adding a “2” in front of the flag. We have classified with flag = -10 objects in slits with a clear observational problem, like e.g. objects for which the automated spectra extraction algorithm in VIPGI (Scodreggio et al. 2005) failed, or objects too close to the edge of a slit to allow for a proper sky subtraction. In the following, redshifts with a flag between 2 and 9 (or 12 and 19 in the case of AGN) are referred to as secure redshifts.

3.1. Data quality

When conducting a large spectroscopic survey, carried out over years, under different weather conditions, and with different people involved at different times in the data reduction and redshift measurement process, it is important to identify an objective way to assess the quality of the data and of the reduction process, independent on the redshift measurement success or failure. For the VVDS Deep and Wide surveys, we have devised a

method which takes into account the most important observational/reduction factors.

Slit obscuration due to field vignetting, effective exposure time, seeing and sky transparency directly impact on the number of photons collected for each spectrum; sky brightness at constant exposure time determines the S/N ratio, and the quality of the wavelength calibration has an impact on the accuracy of the redshift measurement. The goal we set was to devise an objective quality parameter which could be used to make an a priori selection of the best data at hand. The final figure of merit we assigned to each spectrum is the combination of all these factors in such a way that the highest is the figure of merit, the highest the spectrum quality. In the following, we shall discuss in turn each separate contribution to this quality parameter, show the overall results for both surveys and relate it to the redshift confidence level.

3.1.1. Slit obscuration

VIMOS takes advantage of the full Nasmyth field of view, but, due to the design of the guiding probe, a fraction of the field of view can be partially vignetted for some positions of the guiding star. This has happened especially during the first observations, before enough experience had been gained on the choice of the guiding star. Obscured slits can be easily identified by looking at the average level of sky counts in each slit, and comparing it with the average sky level for all the slits in the quadrant. When the single slit has a sky level which is lower than 70% the average sky level, the slit has been flagged as “bad” assigning to it an $obscur_{\text{flag}} = 0$. This happens for a total of 75 objects in the VVDS Deep data, and 181 in the VVDS Wide data. An *a posteriori* check shows that these slits account for 68% and 50% of the spectra where no object is detected in the VVDS Deep and VVDS Wide sample respectively. As all the contributions to the quality parameter are eventually combined in a multiplicative way, all obscured slits will end up in a global quality parameter equal to zero.

3.1.2. Wavelength calibration

As described in Scodeggio et al. (2005), wavelength calibration is performed using both a global fitting, and a slit per slit refinement. For some particular slits towards the edge of the field of view, and in particularly unfavourable positions of the instrument during the observation, flexures can be important, and it is not possible to get a wavelength calibration of the same quality as usual. Using the wavelength calibration rms for each slit (see Scodeggio et al. 2005) as a measure of the wavelength calibration quality, we can identify such deviant cases. The distribution of the wavelength calibration rms for the VVDS Deep (solid line) and the VVDS Wide (dotted line) survey spectra is shown in Fig. 2. There is a small number of slits (1% both in the VVDS Deep survey, and in the VVDS Wide survey) showing a wavelength calibration rms above 6\AA , which essentially means that wavelength calibration has totally failed. Such slits get a “wavelength calibration quality flag” $\lambda_{\text{flag}} = 0$. Furthermore, for some pointings the arc calibration exposure was not usable, and we were forced to calibrate the corresponding spectra using the sky lines. In such cases, the wavelength calibration is never as good as in the standard case, since the sky lines are often broad and/or unresolved at our resolution. This is reflected by the distribution of the wavelength calibration rms for that specific quadrant/pointing, which peaks at $\sim 3.5\text{\AA}$ rather than the usual 1.2\AA .

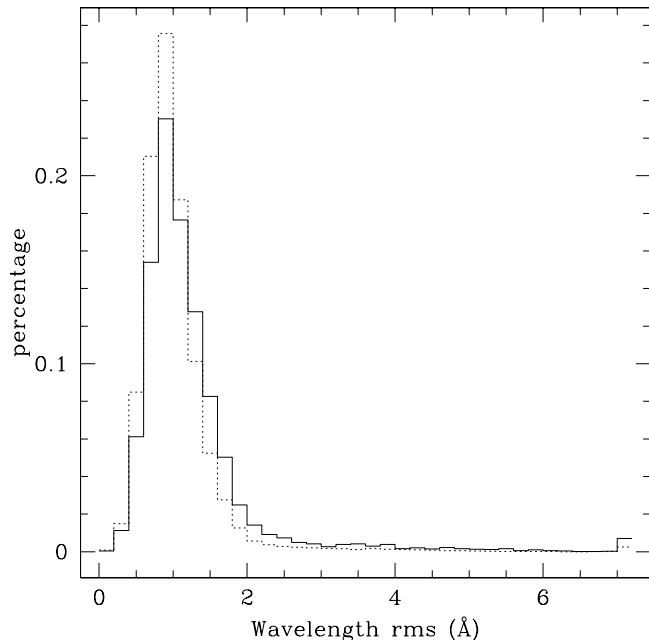


Fig. 2. Distribution of the wavelength calibration rms: VVDS Deep survey, solid histogram, VVDS Wide survey, dotted histogram

We have considered these slits as an intermediate category, and assigned to them a wavelength calibration quality flag of -1. As all the contributions to the quality parameter are eventually combined in a multiplicative way, a shaky ($rms > 3\text{\AA}$) or bad ($rms > 6\text{\AA}$) wavelength calibration will end up in a global quality parameter being negative or equal to zero respectively.

3.1.3. Sky brightness

Sky brightness depends (at zero order) on moon phase and moon distance. In principle, knowing these two parameters and using some calibration table, the expected sky brightness could be computed. In practice, as we are interested in the global background level, a simpler approach has been adopted:

1. for each slit, the mean one dimensional sky spectrum is obtained by taking the median over the sky two-dimensional image along the spatial direction, to reject border effects;
2. after having discarded obscured slits (see 3.1.1), all one dimensional sky spectra are combined and the median sky spectrum for the whole quadrant derived;
3. such median sky spectrum is then normalized for the exposure time and integrated over the full wavelength range to get the median sky value for that quadrant in that pointing (med_{sky});
4. by comparing the median sky values obtained for the same quadrant in the different pointings, we define a “reference sky value” (ref_{sky}) as the mean of the three lowest “median sky values”;
5. finally, the median sky value per quadrant per pointing is compared to ref_{sky} for that quadrant, and a sky quality factor is defined as

$$sky_{\text{qual}} = \frac{1}{\sqrt{\frac{med_{\text{sky}}}{ref_{\text{sky}}}}}$$

In Fig. 3, top left, the distribution of the sky quality parameter for the VVDS Deep (solid line) and VVDS Wide (dotted line) surveys is shown. Overall, the VVDS Wide Survey shows a sky quality parameter distribution broader than the VVDS Deep survey. This is expected, as the VVDS Deep survey observations have been carried out during dark time, while the VVDS Wide survey ones have been partially performed during grey time.

3.1.4. Exposure Time

The exposure time for each pointing of the VVDS Deep survey had been planned to be 16200 seconds, while for the Wide it should have been 2700 seconds per pointing. As a matter of fact, in some cases the effective exposure time has been less than what foreseen, mainly because meteorological conditions had badly deteriorated during the observation, and of course exposure time has a direct impact on the signal to noise ratio as a multiplicative factor. There are also a few observations, performed during visitor runs, which have been lengthened in the attempt to compensate for high airmass or unstable meteorological conditions. By comparing the actual total exposure time of each quadrant in each pointing (obs_{time}), to the nominal exposure time “a priori” established for the survey (ref_{time}), we can define

$$time_{qual} = \sqrt{\frac{obs_{time}}{ref_{time}}}$$

In Fig. 3, top right, the distribution of the Exposure Time quality parameter for the VVDS Deep (solid line) and VVDS Wide (dotted line) surveys is shown. For the vast majority of the pointings, the exposure time effectively used is what had been foreseen for that depth.

3.1.5. Sky Transparency, seeing and slit losses

Atmospheric conditions have a direct influence on sky transparency and seeing, which in turn, and coupled with slit losses, contribute to flux losses in a way which is not possible to disentangle. In order to estimate their global contribution, an empirical approach has been adopted: for each object, we have integrated its spectrum under the I filter response curve, and compared the thus obtained $Iflux_{spectro}$ to the equivalent quantity as obtained from photometry ($Iflux_{phot}$). Then one could in principle compute in one shot the effect of seeing, slit losses and transparency on S/N as

$$mag_{qual} = \sqrt{\frac{Iflux_{spectro}}{Iflux_{phot}}}$$

Such ratio should always be below one, by definition, but, as shown in Le Fèvre et al. (2005c), a small fraction (around few percent) of objects have a value of mag_{qual} above 1.0. This is due to a number of second-order effects affecting the measure, such as: 1) $Iflux_{spectro}$ is affected by how well zero orders or fringing residuals have been removed; 2) $Iflux_{phot}$ has its own errors, larger for fainter magnitudes (0.2 mag for objects fainter than $I_{AB} \sim 23$, for the VVDS Deep survey, McCracken et al. (2003)); 3) the brighter and more extended the object, the more inaccurate is the sky subtraction: the sky region that can be used to compute the sky level is small and dominated by pixels affected by slit edge effects. This can lead to an underestimate of the sky level. This more often occurs in the VVDS Wide survey pointings, where the fraction of brighter (\sim larger) objects is higher, and/or in bad seeing conditions. To quantify the overall

contribution of such second order effects, we can define

$$\frac{Iflux_{spectro}}{Iflux_{phot}} = transmission + residuals$$

where *transmission* is actually due to sky transparency and seeing/slit width ratio, and, for pointlike sources, should be constant within one observation. *residuals* represent the contribution of all the second order effects like those listed above, and as such can vary from object to object. In optimal atmospheric conditions, we should have *transmission* \sim 1 and *residuals* = 0. Indeed, in the magnitude range between $I_{AB} \sim 21.5$ and $I_{AB} \sim 22.5$, where the error on photometric magnitude is negligible and object sizes are small enough not to be affected by slit losses, or to hamper a good background estimate, the mean flux ratio is always below one, being affected by sky transparency only. Thus, on a per quadrant and per pointing basis, using only the range $21.5 \leq I_{AB} \leq 22.5$ we can compute the mean transmission as

$$transmission = \langle \frac{Iflux_{spectro}}{Iflux_{phot}} \rangle$$

Subsequently, and for each object *i* for which $Iflux_{spectro}(i)/Iflux_{phot}(i)$ is above one, we can estimate the residuals as

$$residuals(i) = \frac{Iflux_{spectro}(i)}{Iflux_{phot}(i)} - transmission$$

Finally, the contribution of all these factors to the observation quality can be computed as

$$mag_{qual}(i) = \sqrt{transmission} * \sqrt{1 - residuals(i)}$$

In Fig. 3, panel *e*, the distribution of the mag_{qual} parameter for the VVDS Deep (solid line) and VVDS Wide (dashed line) surveys is shown. Also objects for which no redshift has been measured are included in this panel. Panel *c* and *d* show the distribution of the same parameter for stars and galaxies separately. Comparing the two distributions obtained for stars, we see that in the VVDS Deep survey most stars have a figure of merit close to 1, while for the VVDS Wide survey the peak is around 0.8. As stars are less affected by slit losses than galaxies, panel *c* tells us that the overall better figure of merit for the VVDS Deep survey is mainly due to the better average atmospheric conditions during observations.

3.1.6. Global quality parameter

The above quality parameters have been computed for each object and combined in a multiplicative way as

$$qual = obscur_{flag} * \lambda_{flag} * sky_{qual} * time_{qual} * mag_{qual}$$

The resulting distribution is shown in Fig. 3 bottom panels, for the VVDS Deep (solid line) and VVDS Wide (dotted line) data. Negative values of quality pertain to objects with poor wavelength calibration, while a quality parameter of 0 is due to either bad wavelength calibration or to obscured slits. From Fig. 3, panel *h*, it is apparent that the global distribution of the quality parameter is (slightly) better for the VVDS Deep survey data than for the VVDS Wide survey data. This is essentially due to the mag_{qual} parameter, which is better for the deep survey, while the VVDS Wide survey, in which large and extended galaxies are more abundant, is globally more affected by slit loss effects.

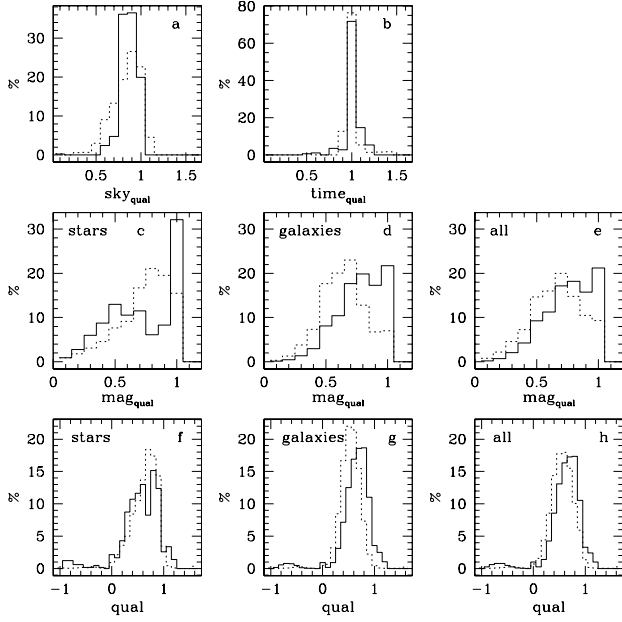


Fig. 3. Distribution of the different contributions to the quality parameter and of the resulting figure of merit for the VVDS Deep (solid line) and VVDS Wide (dashed line) surveys. Panel (a): sky_{qual} ; (b) $time_{qual}$; (c) mag_{qual} for spectroscopic stars; (d) mag_{qual} for galaxies; (e) mag_{qual} for the total sample (including failed redshift measurements); (f) figure of merit for stars and (g) for galaxies; (h) figure of merit for the whole sample (including failed redshift measurements).

The percentage of galaxies with quality above 0.5 is 79% in the VVDS Deep sample and 58% in the VVDS Wide sample. We note, however, that the quality parameter is not an absolute measure of data quality, but just a relative one: it allows to select the best quality spectra we have in our samples (i.e. those for which slit losses are small, observed for the nominal exposure time in excellent atmospheric conditions), or conversely, to discard those data for which something during observations or reduction went wrong. We will see in the following section that this does not necessarily prevent, nor assures, 100% reliable redshift measurements.

3.1.7. Data quality parameter and redshift flag

Once the global quality parameter is obtained, it is interesting to see how it relates to the redshift flag. If both estimates are reliable, we expect that objects with a bad value of the quality parameter (i.e. below 0.5) should have a higher probability of an unsuccessful redshift measurement (flag = 0), while objects with a good value of the quality parameter (above 0.5) should have a higher probability of a very secure redshift flag (i.e. 3 or 4). Still, we do not expect the opposite to be totally true, i.e. there may exist spectra with a not so good quality but to which the redshift can be securely assigned: in fact, the quality parameter is related to the continuum intensity, its signal to noise, and the absolute flux calibration of the data, while the flag is a measure of the reliability of the redshift, and is strongly affected by the presence, or absence, of prominent emission/absorption lines.

In Fig 4, for each flag, the distribution of the quality parameter is shown for the VVDS Deep (left) and VVDS Wide (right)

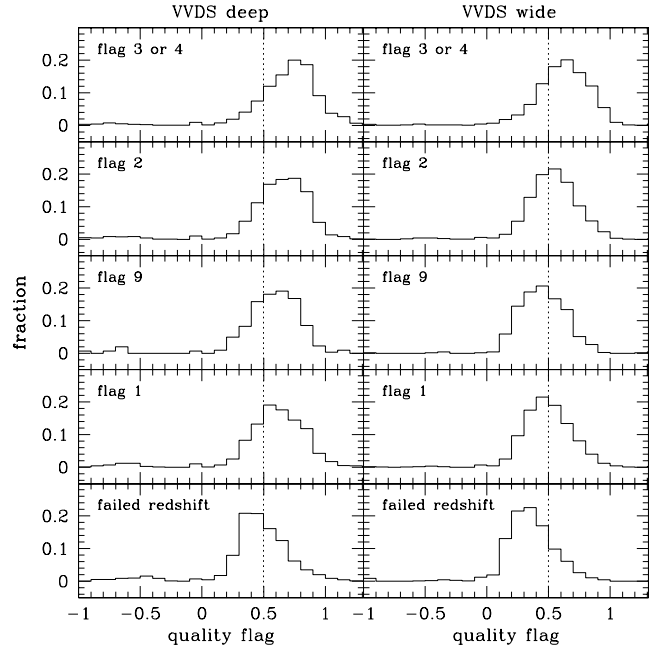


Fig. 4. Distribution of the quality parameter for the VVDS Deep survey, divided by flag: the dotted line indicates the 0.5 value of the quality parameter

surveys. The dotted line indicates the 0.5 value of the quality parameter. As expected, more secure flags are assigned to objects showing, on average, a higher quality parameter, as shown by the peak of the histogram moving towards higher values of quality going to more secure flags. An exception are the flag 9 objects, which show a distribution of the quality parameter comparable to that of the flag 1 objects. This is not a surprise: we recall that a flag 9 is assigned when one secure single spectral feature in emission is visible, and, as anticipated before, an emission line, if strong enough, can be detected even in presence of low S/N continuum, or residual fringing patterns.

More quantitatively, in the VVDS Deep survey only 42% of the failed spectra have a quality parameter larger than 0.5, a percentage which goes down to 20% for the Wide survey. On the other hand, 82% of the objects with a very secure redshift flag (flag 3 or 4) in the Deep survey are derived from spectra of good quality (quality > 0.5), a percentage which decreases to 73% in the Wide case.

Thus, the quality parameter statistically strengthens the redshift flag, and justifies it on the basis of the quality of the data. Furthermore, the coupling of the two pieces of information allows one to easily select subsamples of objects for which not only the redshift has the highest degree of reliability, but the data are above a given quality and thus particularly suitable for detailed studies of the continuum emission.

4. General properties of the spectroscopic sample

In Table 2 we summarize the statistics of redshift measurement for the VVDS Wide sample. For reference, we also report the redshift statistics for the VVDS Deep sample, once it is cut at a limiting magnitude of $I_{AB} \sim 22.5$. So far, in the 3 Wide survey fields we have accumulated 28166 spectra for primary targets, including 16670 galaxies, 258 QSOs and 9164 stars. There are only 2074 spectra for which the redshift measurement failed; this

Table 2. Statistics of redshift quality flags for VVDS Wide sample

Field/flag	primary targets						secondary targets						Total
	0	1	2	3	4	9	20	21	22	23	24	29	
VVDS-F02	38	177	506	798	1501	21	49	26	44	23	28	6	3217
galaxies	-	144	434	708	1121	18	-	25	41	21	23	4	2539
QSOs	-	3	1	12	18	3	-	0	0	0	0	2	39
stars	-	30	71	78	362	-	-	1	3	2	5	-	552
VVDS-F10	327	683	916	674	961	98	85	20	21	12	16	8	3821
galaxies	-	613	772	506	413	94	-	19	18	7	8	8	2458
QSOs	-	6	15	17	3	4	-	0	0	0	0	0	45
stars	-	64	129	151	545	-	-	1	3	5	8	-	906
VVDS-F14	240	669	1241	1268	1845	116	117	59	51	19	32	12	5669
galaxies	-	572	935	893	915	105	-	55	36	16	13	12	3552
QSOs	-	12	9	14	5	11	-	0	2	0	0	0	53
stars	-	85	297	361	925	-	-	4	13	3	19	0	1707
VVDS-F22	1507	2846	4783	3822	5671	499	377	153	122	106	95	46	20027
galaxies	-	2504	3626	2357	1904	461	-	123	99	79	29	46	11228
QSOs	-	22	27	36	39	38	-	1	1	1	2	0	167
stars	-	320	1130	1429	3728	-	-	29	22	26	64	0	6748

corresponds to a success rate larger than 92%. Secure redshift objects (flag between 2 and 9), are 21894, almost 80% of the sample. Although the magnitude limit is only $I_{AB} = 22.5$, thanks to the large surveyed area ($\sim 5.0 \text{ deg}^2$ of effective area), we have a fairly large sample of rare, luminous galaxies at high redshift: 979 with $1.0 < z < 1.4$ and 225 with $1.4 < z < 2.0$. The highest secure redshift measured for a galaxy is 4.0573, while the highest secure redshift object is a QSO at $z=5.0163$. On top of the targeted sample, we also have 772 additional redshifts of objects accidentally falling within the slit. Adding the data collected in the F02 field limited to $I_{AB} = 22.5$, the VVDS Wide sample comprises almost 20000 galaxies and 304 QSOs with measured redshift over 6.1 deg^2 .

4.1. Magnitudes, sampling rate and redshift distribution

In Fig. 5, the magnitude distribution of the photometric parent catalog (top panels, empty histogram) and of the final spectroscopic sample (top panels, shaded histogram) is shown for the three VVDS Wide areas. For comparison, we show the same plot for the VVDS-Deep F02 field, limited to $I_{AB} = 22.5$. The bottom panels show the fraction of observed over total objects vs. magnitude. In all the three VVDS Wide areas, the fraction of observed objects is between 20% and 25%, over the full magnitude range, very similar to the sampling rate of the VVDS Deep area, once limited at $I_{AB} = 22.5$. The slight trend favouring a better sampling at the faintest magnitude in the F02 field is due to the intrinsic deeper limiting magnitude of the spectroscopic selection in this area, $I_{AB} < 24$, which increases the probability of brighter objects to be discarded in favour of fainter ones (see Bottini et al. 2005).

In Fig. 6, the redshift distributions using all available redshifts (irrespective of flags) for the four different areas are shown. Table 3 shows that there are no statistically significant differences between the $N(z)$ obtained using all redshifts, and the ones obtained using only secure redshifts (i.e. flag 2 to 9, redshift confidence $\geq 80\%$).

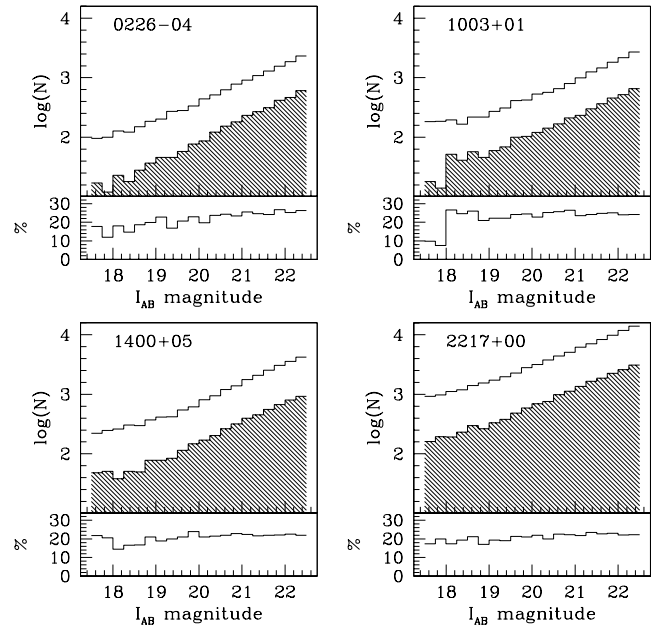


Fig. 5. Spectroscopic survey sampling rate of the four fields as a function of magnitude: in the top panels, the apparent magnitude distribution for the parent photometric catalog (empty histogram) and the observed spectroscopic catalog (shaded histogram); in the bottom panels, the ratio of the two, corresponding to the effective sampling rate as a function of apparent magnitude.

Table 3. Statistics on galaxy redshift distributions ($I_{AB} \leq 22.5$)

Field	all flags			secure flags		
	1 st quartile	median	3 rd quartile	1 st quartile	median	3 rd quartile
F02	0.374	0.611	0.834	0.369	0.611	0.824
F10	0.386	0.616	0.856	0.368	0.605	0.855
F14	0.351	0.560	0.724	0.333	0.559	0.767
F22	0.404	0.571	0.810	0.382	0.560	0.770

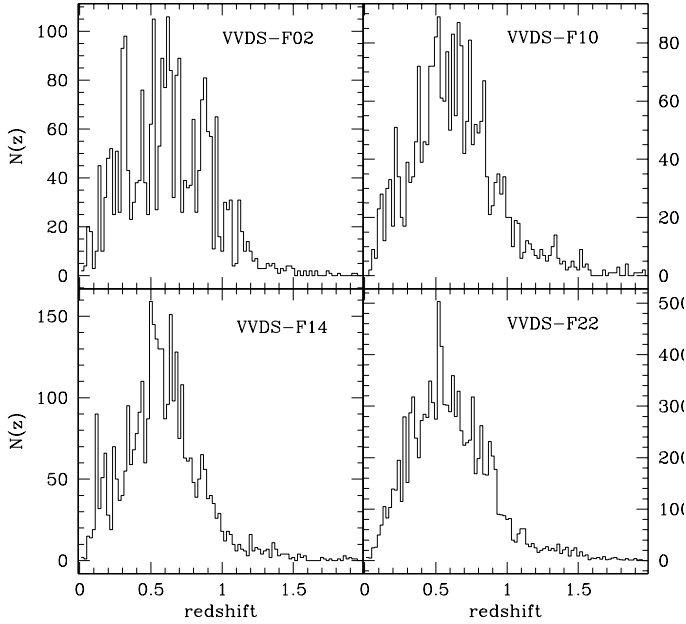


Fig. 6. Observed Redshift distribution to $I_{AB} = 22.5$ in the four VVDS Wide fields, in redshift bins of $\Delta z = 0.02$. All galaxies with quality flag between 1 to 19 have been used.

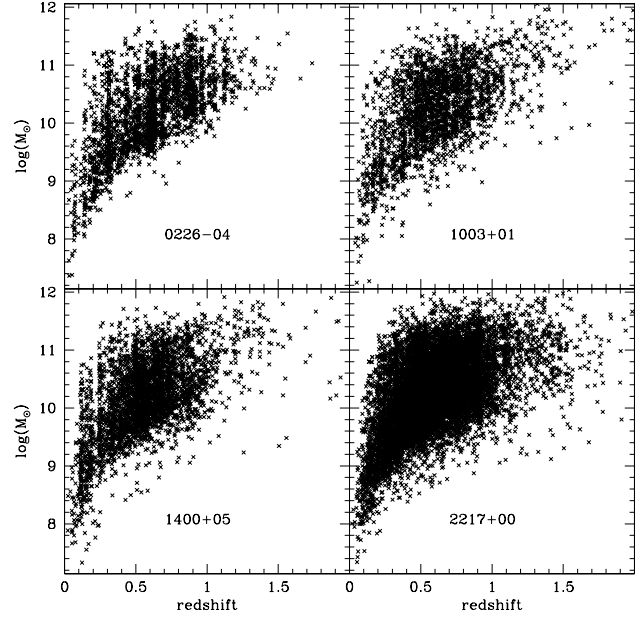


Fig. 8. Stellar mass vs. redshift in the four VVDS Wide areas. The F02 area has been cut to a limiting apparent magnitude $I_{AB} = 22.5$.

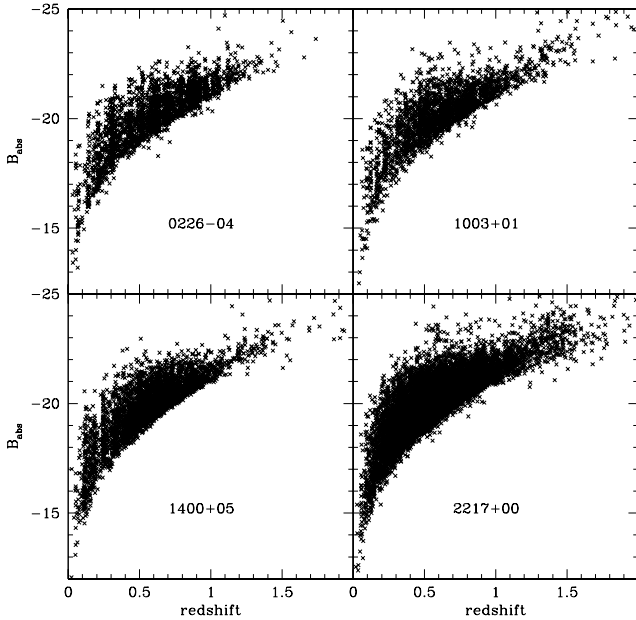


Fig. 7. Absolute B_{AB} magnitude vs. redshift in the four VVDS Wide areas. The F02 area has been cut to a limiting apparent magnitude $I_{AB} = 22.5$

4.2. Galaxy luminosities and stellar masses

The large areas explored, coupled with the relative bright magnitude limit, make the VVDS Wide the ideal survey to explore the bright/massive ends of the luminosity/mass function up to redshift ~ 1 . As an example of the potential of this sample for these studies, in Fig. 7 and 8 we show the absolute B magnitude and stellar mass vs. redshift distribution for the galaxies

with secure redshifts in the four areas. Absolute B magnitudes and stellar masses have been derived by fitting the photometric and spectroscopic data with a grid of stellar population synthesis models generated with the PEGASE2 population synthesis code (Fioc & Rocca-Volmerange 1997), and using the GOSSIP Spectral Energy Distribution tool (Franzetti et al. 2007), where we have adopted a Salpeter IMF and a delayed exponential SFH (see Pozzetti et al. (2007) for a thorough discussion on the dependence of mass values on the different IMF adopted). We can define a unique complete sample of 3542 bright galaxies with $M_{B_{AB}} \leq -21$ up to $z \sim 1$: 2136 galaxies in the F22 field, 412 in F10, 520 in F14, 474 in F02 (we remind that we have cut the F02 area to a limiting apparent magnitude $I_{AB} = 22.5$). At the same limit in redshift, we have more than 11000 galaxies more massive than $\log(M_{\odot})=10$. (6547 galaxies in the F22 field, 1367 in F10, 2009 in F14, 1271 in F02), a sample which will allow a detailed study of the properties of medium to high mass galaxies.

4.3. A direct test of star-galaxy separation techniques

As mentioned earlier, the VVDS was deliberately carried out without any star-galaxy separation prior to spectroscopy. When the survey was planned, only ground based *BVRI* photometry was available (and not over all fields), thus preventing us from using the most efficient color based methods to discriminate between stars and extragalactic objects. Furthermore, the image quality of such ground based photometry was not good enough to apply geometrical arguments discriminate between point-like and extended sources down to the magnitude limits of the Deep and Wide surveys. Thus, we decided to follow the conservative approach of not attempting any *a priori* removal of starlike objects based on colors or compactness. This has led to the high stellar contamination of the spectroscopic sample (up to $\sim 1/3$ for the lower galactic latitude fields). Using UKIDSS K photometry, and CFHTLS *z* photometry available in the F22 and F02

field, we can test with excellent statistics the performances of these star identification methods. We thus applied to the spectroscopic sample the BzK criterium described in Daddi et al. (2004), coupled with a compactness criterium based on the stellarity index provided by *Sextractor*: any object with a stellarity index above or equal 0.9 is catalogued as compact. An object is considered as a star if both criteria are satisfied. To optimize the test, we used only objects with secure redshift (redshift flag > 1) and small photometric errors ($\text{err} < 0.1$) in the B, K and z Bands. Applying this technique to the F02 data (which are deeper and at high galactic latitude), we end up with a residual stellar contamination of only $\sim 2\%$. In the F22 field, which has a brighter magnitude limit and is located at lower galactic latitude, the residual contamination decreases from 35% to 14%. The price to be paid in terms of galaxies which would have been *a priori* discarded is about 5% in the F22 field, and about 2% in the F02 case. We have checked which kind of galaxies were typically discarded and found out that they have the spectrum of a normal elliptical galaxy. Overall, we can state on the basis of observed data that the performance of these two coupled methods in discarding stars is highly efficient, at the low price of a small loss of normal early type galaxies. In addition, we note that we have applied the colour method in the standard form. Exploring in detail alternative color-color selections using the other available bands is beyond the scope of this paper.

5. Large-scale structure and density fluctuations in the VVDS Wide fields

5.1. Galaxy spatial distribution in the F22 field

In Fig. 9 we show the redshift space cone diagram of all galaxies observed in the F22 area, in co-moving coordinates and projected onto the right ascension plane. The figure shows two declination slices, of 1 degree each, to better show the extension of the different structures. Note that the aspect ratio is stretched along the vertical direction. We can identify galaxy overdensities at $z = 0.28, 0.33, 0.41, 0.53, 0.75, 0.82$ and 0.9 , some of which extend over the full surveyed area, both in right ascension and declination: at $z=0.33$ a very thin wall covers the whole field of view of $24 \times 24 \text{ h}^{-1} \text{ Mpc}$; the structure at $z \sim 0.53$ is the most prominent and massive, extending for almost $80 \text{ h}^{-1} \text{ Mpc}$ along the line of sight, and $40 \text{ h}^{-1} \text{ Mpc}$ across. Its presence strongly influences the redshift distribution in this field, lowering its median value and steepening its rise at low redshifts. Such “thick wall” has several subconcentrations, better visible in the slices in declination of Fig. 9. The other visible structures look rather more compact, with a comoving transverse size of the order of $20 \text{ h}^{-1} \text{ Mpc}$, and confined within the 2 square degrees.

5.2. Mean redshift distribution up to $I_{AB} = 22.5$

In terms of their broad shape and peak position, the galaxy redshift distributions in the four areas are relatively similar. At the same time, however, significant field-to-field variations are evident (e.g. the thick wall at 0.53 in the F22 field, as outlined in the previous section). In this and the following sections we quantify this variance and compare it to theoretical expectations, as obtained both from the observed two-point correlation function and from mock surveys built using numerical/semi-analytic models.

Combining the four fields, appropriately taking into account the effective area and the sampling rate of each field, we can derive our current best estimate of the redshift distribution of a mag-

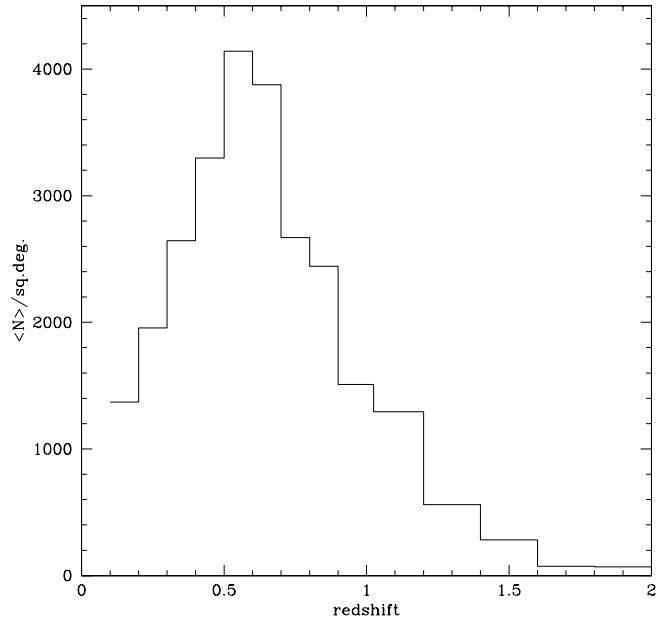


Fig. 10. Mean redshift distribution per square degree obtained in the full survey area of 6.1 square degrees

Table 4. Galaxy surface density as a function of redshift up to a limiting mag $I_{AB} \leq 22.5$ averaged over 6.1 square degrees

z	mean gal/deg ²	max gal/deg ²	min gal/deg ²
0.15	1370	2105	1107
0.25	1956	2635	1356
0.35	2644	3085	2367
0.45	3296	3950	2645
0.55	4142	5123	3346
0.65	3877	4310	3546
0.75	2670	3033	2447
0.85	2443	2980	2089
0.95	1509	1851	1145
1.1	1294	1882	836
1.3	561	746	439
1.5	281	357	193
1.7	74	113	31
1.9	68	108	31

nitude selected sample to $I_{AB} \leq 22.5$. The result is shown in Figure 10 and the corresponding values are reported in Table 4 for convenience. In this figure and table, we use a binning of $\Delta z=0.1$ up to $z=1$, and 0.2 at higher redshift, in order to smooth out the smaller structures present in the different fields. This represents the most accurate redshift distribution measured to date at these faint magnitudes, based on $\sim 20,000$ galaxies over a total area of 6.1 deg^2 , and it can provide an important reference for galaxy formation models.

5.3. Field to field variations

With this unprecedented area surveyed, it becomes possible to quantify the variations in each of the four fields with respect to this average distribution. This is shown in Fig. 11. The top panel reports the redshift distribution of the four fields, using a $\Delta z=0.1$ binning. For reference, around the peak of the distribu-

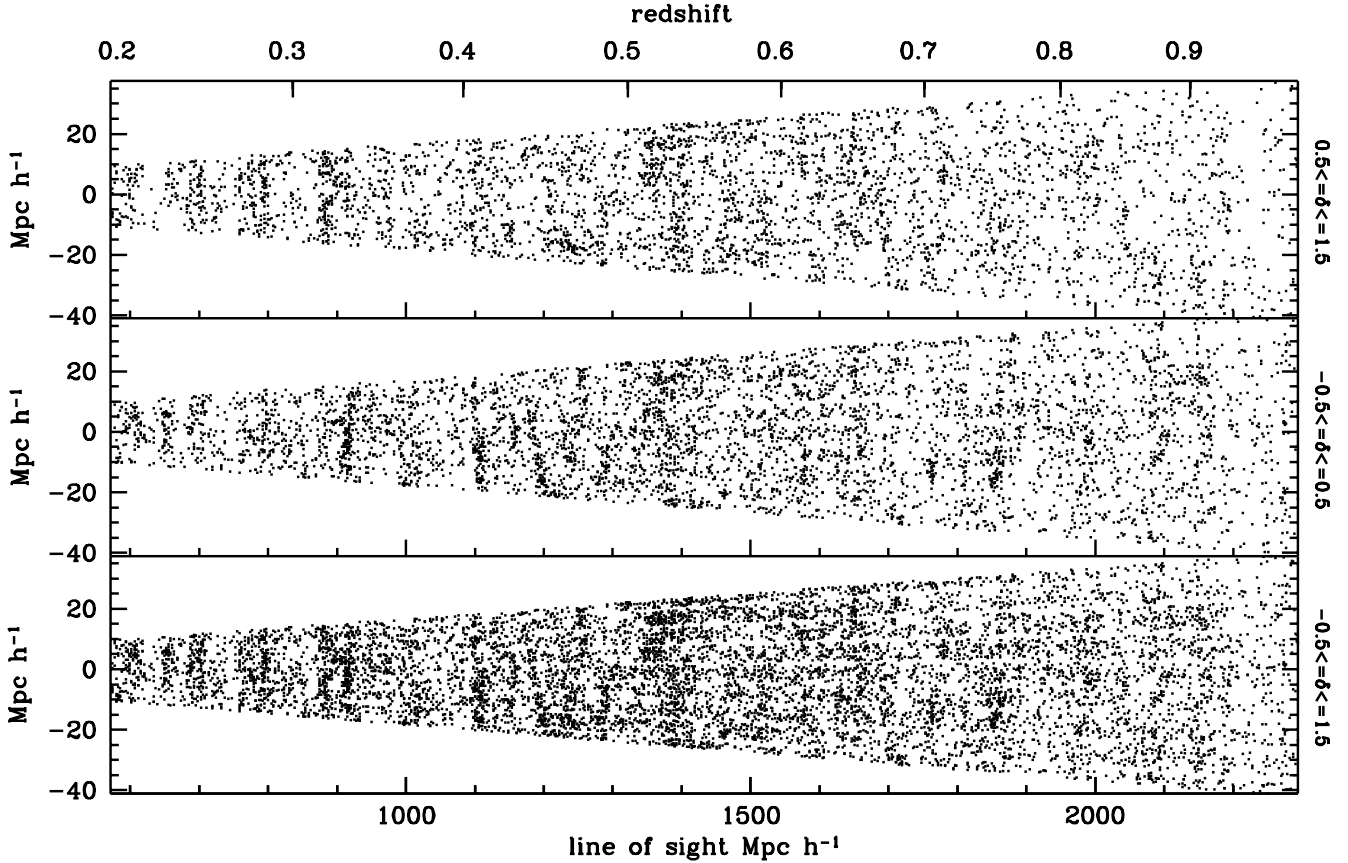


Fig. 9. Cone diagrams of the 3D galaxy distribution in the the F22 field, projected on the right ascension plane for the whole sample (lower panel) and for the two 1 deg slices in declination (upper panels)

tion $z=[0.5,0.6]$ such a redshift bin corresponds to a comoving radial size of $222 \text{ h}^{-1} \text{ Mpc}$. Error bars correspond to Poissonian errors. In the bottom panel of figure 11, we show the fractional difference between the observed $N(z)$ in each field, and the average distribution. This comparison of the fluctuations in the different fields for fixed redshift bins is inevitably qualitative. In fact, given the very different areas covered in the four fields, the same redshift range corresponds to rather different volumes. For example, the smallest field, F02, covers 0.5 deg^2 , i.e. 8 times smaller than the largest one, F22 (4 deg^2). This is certainly one reason for the higher variance in the F02 field (Fig. 11, filled circles).

To properly estimate the intrinsic variance as a function of scale, we have therefore defined a set of square sub-fields over the four survey areas, with increasing angular size. The variance is then computed among the set of N_i homogeneous volumes having identical size on the sky and along the redshift direction. The result is summarized in Fig. 12. In practice, each sky region (represented by a different color and symbol) has been divided – for a given size – into the largest possible number of subareas that could be accommodated. Galaxy densities have been computed in each sub-field and for different redshift bins, properly correcting for the average sampling of the area. Table 5 shows quantitatively the results illustrated in Fig. 12. For each area size, and each redshift bin, we give the number of sub-fields of that size available, the median value, upper/lower quartiles and maximum and minimum of the observed galaxy density. For the largest area, where only 2 measurements are available, we computed the arithmetic mean instead of the median. For the smaller scales represented

(190 arcmin^2) the observed large fluctuations (up to a factor of four between adjacent areas) are not surprising, as we are essentially looking at scales of the order of a few Mpc. At redshifts approaching unity, and for large angular sizes (30 arcmin correspond to $10 \text{ h}^{-1} \text{ Mpc}$ at this redshift) the spread can still be a factor of 2, an indication that important structures exist and are not uncommon at such redshift. It is interesting to see, using the larger areas, how much variance we expect in a field of 0.5 deg^2 (1800 square arcminutes) like F02, i.e. the field of the VVDS-Deep survey. For example, at redshift 0.75 we still see peak to peak fluctuations of $\sim 30 \%$ in the counts. We also notice a significant excess fluctuation in the data from the field F22 (red circles) in the redshift bin 0.5-0.6. In particular, all counts are shifted towards higher values, reflecting the presence of the global large-scale fluctuation covering the full field already mentioned in section 5.1.

5.4. Measuring cosmic variance

The results of Fig. 12 can be translated from the observational space into a framework which is theoretically easier to interpret in terms of cosmic variance and expectations from galaxy clustering. Given a set of N identical volumes with volume V , we can define the observed variance among them as

$$\sigma_v^2 = \frac{\langle N^2 \rangle - \langle N \rangle^2}{\langle N \rangle^2} = \frac{1}{\langle N \rangle} \quad (1)$$

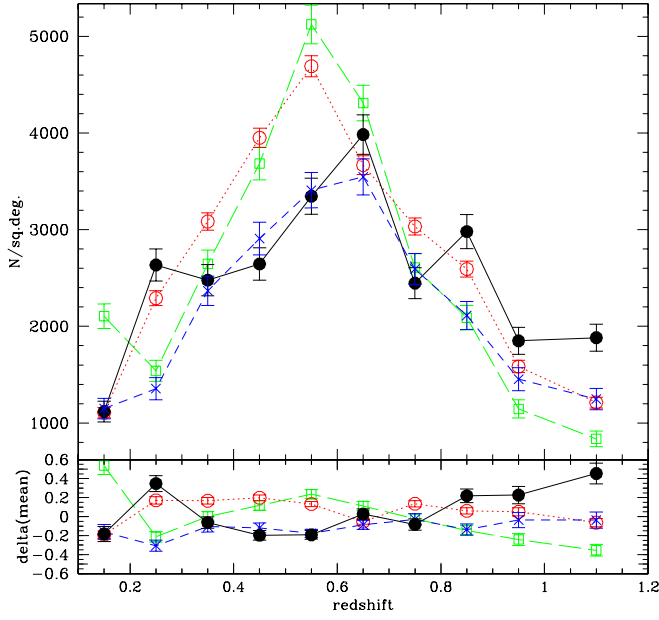


Fig. 11. Top: Redshift distribution (in galaxies per unit effective area) in the four VVDS-Wide areas: F02, black dots and solid line, F10 blue crosses and short dashed line, F14 green squares and long dashed line, and F22, red circles and dotted line. The sampling corrections have been assumed to be independent of redshift. Bottom: field-to-field variations, relative to the globally averaged redshift distribution of figure 10.

(e.g. Somerville et al. (2004)), where the last term is the correction for Poissonian shot noise. In the following we will compute σ_v^2 following eq. 1 only when the Poisson shot noise is smaller than 10%. The observed variance in the counts at a given redshift can be compared to that expected from the two-point correlation function of the galaxy sample. Following (Peebles 1980)

$$\sigma_v^2 = \frac{1}{V^2} \int_V d^3x_1 d^3x_2 \xi(|\mathbf{x}_1 - \mathbf{x}_2|) \quad (2)$$

If the galaxy correlation function can be described as a power law, $\xi(r) = (r/r_0)^{-\gamma}$, then this expression becomes

$$\sigma_v^2 = J_2 (r_0/r)^\gamma \quad (3)$$

where $J_2 = 72.0/[(3-\gamma)(4-\gamma)(6-\gamma)2^\gamma]$ and r_0 and γ are measured from the observations.

Following the same approach as in Le Fèvre et al. (2005a), and using the VVDS-Deep F02 data limited at $I_{AB} \leq 22.5$, we have estimated the best fit correlation function parameters in different redshift bins, and used eq. 3 to check whether the observed variance measured from the field-to-field scatter (as from eq. 1) can be recovered consistently by extrapolating the correlation function measured from a much smaller field. The results are shown in Fig. 13, where we plot the observed square-root σ_v of the variance (i.e. the value of the *rms* fluctuation) against the volume. The red asterisks correspond to the direct measurement, obtained from the scatter among N_i samples within the given volume. The dashed area shows the same quantity as obtained using the 3σ confidence intervals of the VVDS-Deep F02 correlation function (limited at $I_{AB} \leq 22.5$).

One notices immediately that the variance directly estimated from the galaxy counts in the different fields is in excellent

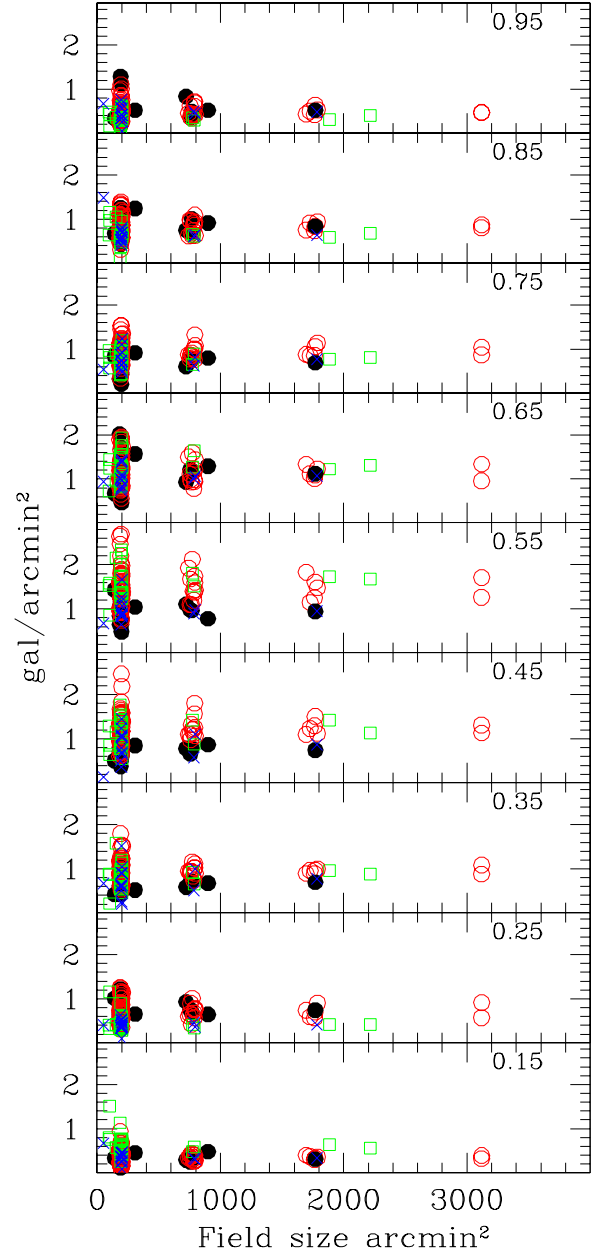


Fig. 12. A different view of the galaxy redshift distribution, evidencing the effect of varying the field size. The ascissa shows the size of the field on the sky in square arcminutes, while the ordinate gives the corresponding value of the surface density (in galaxies per unit area) in the given redshift bin of size $\Delta z = 0.1$ (centered at the mean redshift given in each panel). Sub-fields of increasing size are coded according to their parent VVDS-Wide field: F02 (black dots), F10 (blue crosses) F14 (green squares) and F22 (red circles). Clearly, the largest-size sub-fields can only be drawn from the largest parent field, i.e. F22. Statistical errors on each measurement are of the same size as the symbols.

agreement with the cosmic variance as estimated from the correlation function. Only at redshift 0.35 and 0.65 and for volumes of $\sim 10^5 h^{-1} Mpc^3$, field to field variance appears smaller than the one predicted from the correlation function parameters. Looking back at the distribution of the number counts (fig. 11), at these

Table 5. Galaxy density median values and spread in different area sizes at different redshifts

$\langle z \rangle$	area arcmin ²	N areas	median	upper quartile	lower quartile	max	min
0.15	190	96	0.37	0.52	0.25	0.67	0.18
0.25	190	96	0.61	0.82	0.45	1.07	0.35
0.35	190	96	0.86	1.05	0.62	1.23	0.50
0.45	190	96	1.03	1.38	0.77	1.57	0.60
0.55	190	96	1.32	1.63	1.01	1.98	0.79
0.65	190	96	1.10	1.43	0.94	1.70	0.79
0.75	190	96	0.82	1.05	0.67	1.19	0.50
0.85	190	96	0.74	0.96	0.59	1.15	0.51
0.95	190	96	0.45	0.58	0.32	0.75	0.25
0.15	780	19	0.34	0.42	0.29	0.48	0.26
0.25	780	19	0.66	0.76	0.45	0.93	0.36
0.35	780	19	0.92	1.00	0.69	1.12	0.59
0.45	780	19	1.10	1.26	0.87	1.57	0.66
0.55	780	19	1.38	1.67	0.98	1.92	0.89
0.65	780	19	1.14	1.29	0.98	1.59	0.93
0.75	780	19	0.81	0.91	0.76	1.08	0.62
0.85	780	19	0.75	0.94	0.63	1.01	0.62
0.95	780	19	0.45	0.61	0.38	0.72	0.35
0.15	1725	8	0.36	0.40	0.33	0.64	0.30
0.25	1725	8	0.70	0.74	0.56	0.91	0.41
0.35	1725	8	0.96	0.97	0.89	1.00	0.70
0.45	1725	8	1.24	1.42	1.10	1.51	0.75
0.55	1725	8	1.45	1.73	1.15	1.83	0.94
0.65	1725	8	1.12	1.23	1.09	1.33	1.01
0.75	1725	8	0.85	1.05	0.77	1.14	0.69
0.85	1725	8	0.83	0.91	0.74	0.94	0.59
0.95	1725	8	0.50	0.53	0.44	0.64	0.31
0.15	3120	2	0.35	-	-	0.39	0.32
0.25	3120	2	0.74	-	-	0.91	0.57
0.35	3120	2	0.98	-	-	1.08	0.88
0.45	3120	2	1.22	-	-	1.31	1.13
0.55	3120	2	1.48	-	-	1.71	1.26
0.65	3120	2	1.15	-	-	1.34	0.96
0.75	3120	2	0.95	-	-	1.04	0.87
0.85	3120	2	0.83	-	-	0.87	0.80
0.95	3120	2	0.47	-	-	0.47	0.47

two redshifts we note a remarkable similarity among the different fields, as well as in the galaxy surface density distribution in fig. 12 and table 5. This similarity automatically converts in a lower field to field variance, which in any case remains compatible with the one computed from correlation function at a 1.2 σ level.

Using 100 quasi-independent mock samples of 2×2 degrees (for details, see Guzzo et al. 2008) built applying to the Millennium simulation (Springel et al. 2005; Blaizot et al. 2005) the semi-analytic prescription of De Lucia & Blaizot (2007), we have computed model predictions for cosmic variance again using eq. 1. The model predictions (green filled squares) are quite well consistent with the observed field-to-field variance, with a difference which is at most 1.5 σ at $z=0.65$ for volumes of $\sim 10^5$ $h^{-1} Mpc^3$.

6. Public Data Release and Database Access

We are publicly releasing all redshift measurements in the F22 area through the CENCOS (CENtre de COSmologie) database environment on our web site <http://cencosw.oamp.fr> with access to the database built under the Oracle environment, and through VO services (VVDS_WIDE ConeSearch service). The catalog can be searched by coordinates, redshift interval, identification

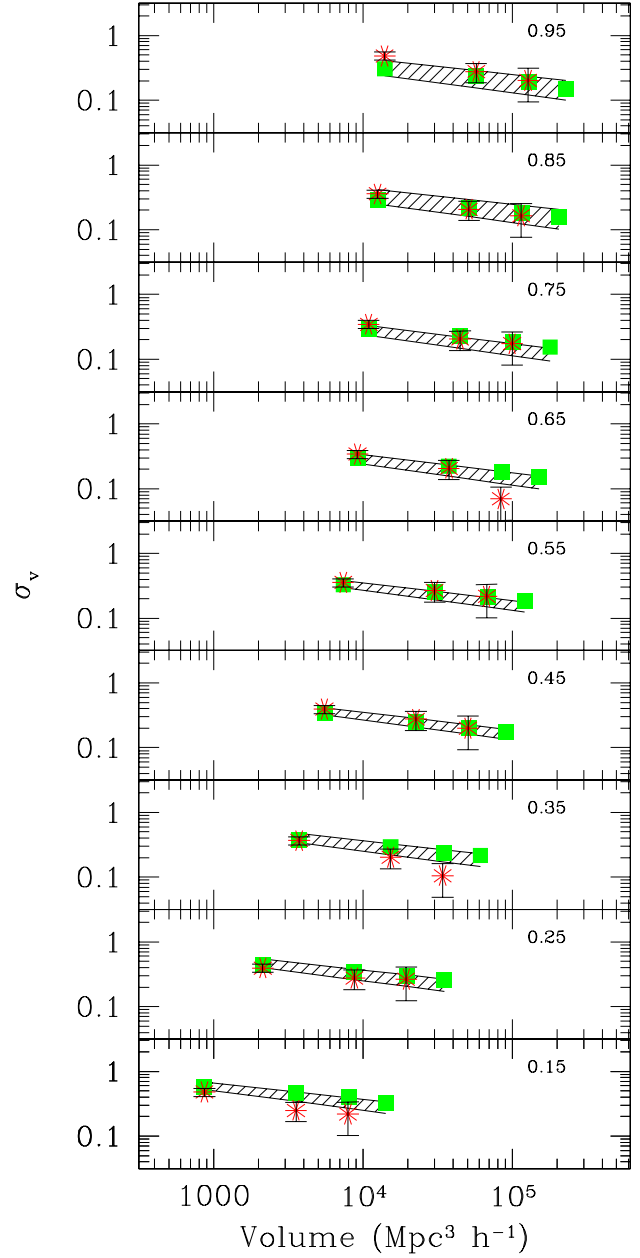


Fig. 13. Comparison of the *rms* number density fluctuation (the square-root of the variance) among independent sub-areas of different size drawn from the four VVDS-Wide survey fields (red asterisks), with that predicted on the basis of the galaxy two-point correlation function (dashed bands). This is shown as a function of redshift (see insets). The green filled squares give the same directly measured *rms* fluctuations from the Millennium mock samples.

number, in combination with the spectra quality flags. Spectra in FITS format are already available on the same site (or through VO SSA service) for the F02 area, both from the CENCOS site and the VO SSA service VVDS_F02_DEEP. The remaining redshifts, together with all spectra in FITS format, will be available as soon as the whole set of available data will be measured.

7. Summary

The VVDS Wide survey is still ongoing but it has already measured redshifts for 26864 objects (including serendipitous objects) in 3 areas covering a total of 5.6 deg^2 to a limiting magnitude of $I_{AB} = 22.5$, to which we can add 3130 redshifts to the same limiting magnitude obtained by the VVDS Deep survey in the F02 field. The success rate in redshift measurement is more than 92% and more than three quarters of the redshifts have a confidence higher than 80%. Overall (i.e. including the F02 field and serendipitous objects) the current sample includes 19777 galaxies, 304 broad line QSOs, and 9913 stars, while the total area covered amounts to 6.1 deg^2 . When completed, the total area coverage will be of 8.6 deg^2 , and the total number of redshifts of the order of 50000.

The large number of redshifts available in the F22 field, coupled with a sampling rate of $\sim 23\%$, allows to identify and describe several prominent structures present along the line of sight up to $2500 \text{ h}^{-1} \text{ Mpc}$. Typical sizes are of the order of $20 \text{ h}^{-1} \text{ Mpc}$, but one large clumpy structure extends for almost $80 \text{ h}^{-1} \text{ Mpc}$ along the line of sight, and $40 \text{ h}^{-1} \text{ Mpc}$ across.

We give the mean $N(z)$ distribution averaged over 6.1 deg^2 (fig. 10) for a sample limited in magnitude to $I_{AB} = 22.5$. We have estimated field to field variations in terms of number counts (see fig. 11 and table 4) and galaxy surface density both as a function of field size and redshift (see fig. 12 and table 5), showing that differences as high as a factor of two can exist at $z=1$ for still relatively large scales of the order 30 arcminutes, like those considered in many deep surveys today. For fields limited to smaller scales (of the order 10 arcminutes), the spread in galaxy densities can be up to a factor 2.5. Still, the observed cosmic variance is consistent both with what derived from the correlation function parameters, and from theoretical simulations (see fig.13). In addition to the evolution of clustering and large-scale structure, this data set is best suited to study in detail the bright end of the luminosity function, as well as the massive end of the mass function, up to $z \sim 1$ in four different fields observed with identical purely magnitude limited selection.

The redshift catalog for the F22 area is available at the web site <http://cencosw.oamp.fr>, or via ConeSearch VO service *VVDS_WIDE*.

Acknowledgements. This research has been developed within the framework of the VVDS consortium.

This work has been partially supported by the CNRS-INSU and its Programme National de Cosmologie (France), and by Italian Ministry (MIUR) grants COFIN2000 (MM02037133) and COFIN2003 (num.2003020150) and by INAF grants (PRIN-INAf 2005).

The VLT-VIMOS observations have been carried out on guaranteed time (GTO) allocated by the European Southern Observatory (ESO) to the VIRMOS consortium, under a contractual agreement between the Centre National de la Recherche Scientifique of France, heading a consortium of French and Italian institutes, and ESO, to design, manufacture and test the VIMOS instrument.

References

Abazajian, K., Adelman-McCarthy, J. K., Agüeros, M. A., et al. 2003, *AJ*, 126, 2081
 Arnouts, S., Schiminovich, D., Ilbert, O., et al. 2005, *ApJ*, 619, L43
 Blaizot, J., Wadadekar, Y., Guiderdoni, B., et al. 2005, *MNRAS*, 360, 159
 Bondi, M., Ciliegi, P., Zamorani, G., et al. 2003, *A&A*, 403, 857
 Bottini, D., Garilli, B., Maccagni, D., et al. 2005, *PASP*, 117, 996
 Chiappetti, L., Tajer, M., Trinchieri, G., et al. 2005, *A&A*, 439, 413
 Ciliegi, P., Zamorani, G., Bondi, M., et al. 2005, *A&A*, 441, 879
 Colless, M., Dalton, G., Maddox, S., et al. 2001, *MNRAS*, 328, 1039
 Cucciati, O., Iovino, A., Marinoni, C., et al. 2006, *A&A*, 458, 39
 Daddi, E., Cimatti, A., Renzini, A., et al. 2004, *ApJ*, 617, 746
 Davis, M., Faber, S. M., Newman, J., et al. 2003, in *Discoveries and Research Prospects from 6- to 10-Meter-Class Telescopes II*. Edited by Guhathakurta,

Puragra. Proceedings of the SPIE, Volume 4834, pp. 161-172 (2003), 161–172
 De Lucia, G. & Blaizot, J. 2007, *MNRAS*, 375, 2
 Fioc, M. & Rocca-Volmerange, B. 1997, *A&A*, 326, 950
 Franzetti, P., Garilli, B., Fumana, M., et al. 2007, in Proceedings of the ESA Workshop "Astronomical Spectroscopy and the Virtual Observatory,"
 Gialalisco, M., Ferguson, H. C., Koekemoer, A. M., et al. 2004, *ApJ*, 600, L93
 Guzzo, L., Pierleoni, M., Meneux, B., et al. 2008, *Nature*, 451, 541
 Ilbert, O., Cucciati, O., Marinoni, C., et al. 2006, *ArXiv Astrophysics e-prints*
 Ilbert, O., Tresse, L., Zucca, E., et al. 2005, *A&A*, 439, 863
 Iovino, A., McCracken, H. J., Garilli, B., et al. 2005, *A&A*, 442, 423
 Koo, D. 1995, in *Wide Field Spectroscopy and the Distant Universe*, ed. S. J. Maddox & A. Aragon-Salamanca, 55–+
 Le Fèvre, O., Guzzo, L., Meneux, B., et al. 2005a, *A&A*, 439, 877
 Le Fevre, O., Hudon, D., Lilly, S. J., et al. 1996, *ApJ*, 461, 534
 Le Fèvre, O., Paltani, S., Arnouts, S., et al. 2005b, *Nature*, 437, 519
 Le Fèvre, O., Vettolani, G., Garilli, B., et al. 2005c, *A&A*, 439, 845
 LeFevre, O., Saisse, M., Mancini, D., et al. 2003, in Proceedings of the SPIE, ed. M. Iye & A. F. Moorwood, Vol. 4841, 1670–1681
 Li, C., Kauffmann, G., Jing, Y. P., et al. 2006, *MNRAS*, 368, 21
 Lonsdale, C. J., Smith, H. E., Rowan-Robinson, M., et al. 2003, *PASP*, 115, 897
 Madgwick, D. S., Hawkins, E., Lahav, O., et al. 2003, *MNRAS*, 344, 847
 Marinoni, C., Le Fèvre, O., Meneux, B., et al. 2005, *A&A*, 442, 801
 McCracken, H. J., Radovich, M., Bertin, E., et al. 2003, *A&A*, 410, 17
 Meneux, B., Guzzo, L., Garilli, B., et al. 2008, *A&A*, 478, 299
 Meneux, B., Le Fèvre, O., Guzzo, L., et al. 2006, *A&A*, 452, 387
 Norberg, P., Baugh, C. M., Hawkins, E., et al. 2002, *MNRAS*, 332, 827
 Norberg, P., Baugh, C. M., Hawkins, E., et al. 2001, *MNRAS*, 328, 64
 Peebles, P. J. E. 1980, *The large-scale structure of the universe* (Princeton University Press)
 Pierre, M., Valtchanov, I., Altieri, B., et al. 2004, *Journal of Cosmology and Astro-Particle Physics*, 9, 11
 Pollo, A., Guzzo, L., Le Fèvre, O., et al. 2006, *A&A*, 451, 409
 Pozzetti, L., Bolzonella, M., Lamareille, F., et al. 2007, *A&A*, 474, 443
 Radovich, M., Arnaboldi, M., Ripepi, V., et al. 2004, *A&A*, 417, 51
 Schiminovich, D., Ilbert, O., Arnouts, S., et al. 2005, *ApJ*, 619, L47
 Scodeggio, M., Franzetti, P., Garilli, B., et al. 2005, *PASP*, 117, 1284
 Shepherd, C. W., Carlberg, R. G., Yee, H. K. C., et al. 2001, *ApJ*, 560, 72
 Somerville, R. S., Lee, K., Ferguson, H. C., et al. 2004, *ApJ*, 600, L171
 Springel, V., White, S. D. M., Jenkins, A., et al. 2005, *Nature*, 435, 629
 Steidel, C. C., Adelberger, K. L., Dickinson, M., et al. 1998, *ApJ*, 492, 428
 Warren, S. J., Hambly, N. C., Dye, S., et al. 2007, *MNRAS*, 375, 213
 White, S. D. M. & Rees, M. J. 1978, *MNRAS*, 183, 341
 Zehavi, I., Zheng, Z., Weinberg, D. H., et al. 2005, *ApJ*, 630, 1
 Zucca, E., Ilbert, O., Bardelli, S., et al. 2006, *A&A*, 455, 879

¹ INAF-IASF, Via Bassini 15, I-20133, Milano, Italy

² Laboratoire d'Astrophysique de Marseille, UMR 6110 CNRS-Université de Provence, BP8, F-13376 Marseille Cedex 12, France

³ INAF-Osservatorio Astronomico di Bologna, Via Ranzani 1, I-40127, Bologna, Italy

⁴ INAF-IRA, Via Gobetti 101, I-40129, Bologna, Italy

⁵ INAF-Osservatorio Astronomico di Capodimonte, Via Moiriello 16, I-80131, Napoli, Italy Italy

⁶ Università di Bologna, Dipartimento di Astronomia, Via Ranzani 1, I-40127, Bologna, Italy

⁷ Laboratoire d'Astrophysique de Toulouse-Tarbes, Université de Toulouse, CNRS, 14 avenue Edouard Belin, F-31400 Toulouse, France

⁸ Max Planck Institut für Astrophysik, D-85741, Garching, Germany

⁹ INAF-Osservatorio Astronomico di Brera, Via Brera 28, I-20021, Milan, Italy Italy

¹⁰ Institut d'Astrophysique de Paris, UMR 7095, 98 bis Bvd Arago, F-75014, Paris, France

¹¹ Observatoire de Paris, LERMA, 61 Avenue de l'Observatoire, F-75014, Paris, France

¹² Astrophysical Institute Potsdam, An der Sternwarte 16, D-14482, Potsdam, Germany

¹³ INAF-Osservatorio Astronomico di Roma, Via di Frascati 33, I-00040, Monte Porzio Catone, Italy

¹⁴ Università di Milano-Bicocca, Dipartimento di Fisica, Piazza delle Scienze 3, I-20126, Milano, Italy

¹⁵ Integral Science Data Centre, ch. d'Écogia 16, CH-1290, Versoix, Switzerland

¹⁶ Geneva Observatory, ch. des Maillettes 51, CH-1290, Sauverny, Switzerland

¹⁷ Astronomical Observatory of the Jagiellonian University, ul Orla 171, PL-30-244, Kraków, Poland

¹⁸ Centre de Physique Théorique, UMR 6207 CNRS-Université de Provence, F-13288, Marseille, France

¹⁹ Institute for Astronomy, 2680 Woodlawn Dr., University of Hawaii, Honolulu, Hawaii, 96822, USA

²⁰ School of Physics & Astronomy, University of Nottingham, University Park, Nottingham, NG72RD, UK

²¹ Max Planck Institut für Extraterrestrische Physik (MPE), Giessenbachstrasse 1, D-85748 Garching bei München, Germany

²² Canada France Hawaii Telescope corporation, Mamalahoa Hwy, Kamuela, HI-96743, USA

²³ Université de Lyon, Lyon, F-69003, France ; Université Lyon 1, Observatoire de Lyon, 9 avenue Charles André, Saint-Genis Laval, F-69230, France ; CNRS, UMR 5574, Centre de Recherche Astrophysique de Lyon ; Ecole Normale Supérieure de Lyon, Lyon, F-69007, France.